hp**FEM Analysis of Coupled Hyperelasticity and Damage**

Jorge Luis Suzuki

Department of Mechanical Design / Faculty of Mechanical Engineering
State University of Campinas
jlsuzuki@fem.unicamp.br

Marco Lúcio Bittencourt

Department of Mechanical Design / Faculty of Mechanical Engineering
State University of Campinas
mlb@fem.unicamp.br

ABSTRACT

The objective of this work is the application of the high-order hpFEM to the analysis of hyperelastic materials coupled to isotropic damage. A mixed (u/p) formulation with a pressure projection procedure is used in conjunction with the hpFEM to overcome the volumetric locking. The isotropic damage model introduces a scalar variable that evolves coupled with the maximum attained strain. It is based on the equivalent stress concept, by applying a reduction factor over the stress tensor. A cyclic loading test was performed to reproduce the Mullins effect. Convergence analyses were made for a compressible and a quasi-incompressible material imposing analytical solutions. Both materials presented a spectral convergence rate for the p refinement using smooth solutions. In the case of quasi-incompressibility, the material showed locking-free characteristics, but the approximation errors were higher compared to the compressible case.

Keywords: hpFEM, hyperelasticity, damage, volumetric locking.

1 INTRODUCTION

The use of rubber materials is of great relevance for engineering applications. Several phenomenological and mechanistic hyperelastic models were established to describe the material response. Among the first ones were the Neo-Hookean and Mooney-Rivlin models, which use strain energy density functions based on the deformation tensor invariants [7]. The Ogden model was developed in the decade of 1980s, based on the principal directions [20]. A more recent contribution is the Fung material [10], developed in the decade of 1990s. Despite the application for engineering rubber materials, the modeling of soft tissues is of increasing interest, and these material models provide a satisfactory mechanical response [2, 21].

An issue about real applications is the fact that hyperelastic formulations are not able to predict the so called Mullins effect, characterized by the strain induced loss of stiffness observed in experimental tests [6, 19]. The first continuum damage formulation developed for hyperelasticity was the one dimensional Gurtin-Francis model [11]. A generalization of this model for three dimensions was later introduced by [6], keeping the simplicity of the method. Another model, based on the principle

1

of equivalent stress [22] was developed for hyperelasticity and extended to viscoelastic models in a three-dimensional context.

A problem that arises with the treatment of quasi-incompressible hyperelasticity in the Finite Element Method is the volumetric locking. With the enforcement of $\nu \to 0.5$, only very small volumetric deformations are allowed [15]. That yields, for conventional low order FEM formulations, small, moderate or very high errors for the displacements. Additionally, due to the high bulk modulus K, the errors for the stresses become very high [1, 12].

Several solution strategies were proposed to overcome the volumetric locking phenomenon. The most known are the Selective Reduced Integration [9], B-bar method [15] and F-bar method [5]. The methodology used for this work is a mixed (u/p) formulation with a pressure projection procedure, introduced by [4]. The strain energy density is separated into deviatoric and volumetric parts, and the pressure is kinematically coupled to the displacements in a weak sense. A projection is performed at the element level onto an appropriate pressure field, in a least squares sense. This pressure variable is assumed discontinuous between the element boundaries, and thus there is no need to solve it globally [4, 24]. Another advantage relies on the fact that the local treatment for the pressure makes the methodology simpler to implement in a displacement only FEM code.

The pFEM method is a version that uses high order polynomials for interpolation. It provides a locking-free behavior for quasi-incompressible problems [12, 24], and shows spectral convergence rate for smooth solutions [8, 17]. It also permits the usage of elements with higher/lower aspect ratio. The hpFEM considers the combination of higher order polynomials with the increase of the number of elements. Both versions have been used to solve problems of several areas, like fluid and structural mechanics, plasticity, mechanical contact, among others [8, 13, 17, 23, 18].

In this work we used a hp version for treating quasi-incompressible hyperelastic problems with damage. The volumetric locking is avoided with the use of high order polynomials along with the mixed method [4]. The damage is introduced as a scalar variable, following the work of [22, 14] to reproduce the Mullins Effect. The main point relies on the coupled effect of quasi-incompressibility and damage over the approximate solution when increasing the interpolation order.

This work is organized as follows: in Section 2 we present the quasi-incompressible hyperelastic Mooney-Rivlin material with the deviatoric/volumetric separation, followed by the weak formulation and projection procedure [4, 24]. Section 3 presents the applied damage model, the modified stress and the resulting constitutive relations [22, 14]. The obtained results are reported in Section 4, where two main tests were performed. The first focuses the reproduction of the Mullins effect followed by a convergence analysis for a compressible Neo-Hookean material. The second focuses on the convergence of a quasi-incompressible Mooney-Rivlin material with damage, where we imposed a high bulk modulus and analyzed the errors for the displacements, stresses and damage.

2 HYPERELASTICITY

2.1 Quasi-incompressible Mooney-Rivlin material

The strain energy density is written in an uncoupled form, comprising a deviatoric part $\bar{W}$ and a volumetric part $\tilde{W}$ [4]

$$W\left(I_1, I_2, J\right) = \bar{W}\left(I_1, I_2\right) + \tilde{W}\left(J\right), \tag{1}$$

with I_1 and I_2 representing the first and second invariants of $\mathbf{C}$, respectively. The volumetric term is only dependent of the Jacobian J, which derives from the third invariant of $\mathbf{C}$. The expressions for $\bar{W}$ and $\tilde{W}$ are

$$\bar{W}(I_1, I_2) = A_{10}\left(I_1 J^{-2/3} - 3\right) + A_{01}\left(I_2 J^{-4/3} - 3\right), \tag{2}$$

$$\tilde{W}(J) = \frac{K}{2}(J-1)^2, \tag{3}$$

where K is the bulk modulus and A_{10}, A_{01} are the material parameters related to the shear modulus in linear elasticity as

$$G = 2(A_{10} + A_{01}). \tag{4}$$

The hydrostatic pressure is kinematically coupled to the displacements as

$$p = \frac{\partial \tilde{W}}{\partial J}, \tag{5}$$

yielding the following linear relationship

$$p = K(J-1). \tag{6}$$

Following the procedure, the second Piola-Kirchhoff stress tensor represented by

$$\mathbf{S} = \bar{\mathbf{S}} + \tilde{\mathbf{S}}, \tag{7}$$

$$\begin{aligned}
\bar{\mathbf{S}} &= 2A_{10}J^{-2/3}\mathbf{I} + 4A_{01}J^{-4/3}\left(I_1\mathbf{I} - \mathbf{C}\right) \\
&+ \left(-\frac{2}{3}A_{10}I_1 J^{-2/3} - \frac{4}{3}A_{01}I_2 J^{-4/3}\right)\mathbf{C}^{-1},
\end{aligned} \tag{8}$$

$$\tilde{\mathbf{S}} = Jp\mathbf{C}^{-1}. \tag{9}$$

The constitutive tensor $\mathcal{C}$ is decomposed in three distinct terms after the application of the chain rule. One is purely deviatoric $\bar{\mathcal{C}}$, another, $\tilde{\mathcal{C}}^1$ depends directly on the hidrostatic pressure, and the last one $\tilde{\mathcal{C}}^2$ contains the pressure coupled to the displacements by a derivative

$$\bar{\mathcal{C}} = \frac{\partial \bar{\mathbf{S}}}{\partial \mathbf{E}}, \tag{10}$$

$$\tilde{\mathcal{C}}^1 = \frac{\partial\left(J\mathbf{C}^{-1}\right)}{\partial \mathbf{E}}p, \tag{11}$$

$$\tilde{\mathcal{C}}^2 = J\mathbf{C}^{-1}\frac{\partial p}{\partial \mathbf{E}}. \tag{12}$$

2.2 Principle of Virtual Powers (PVP)

The total potential energy written in a total Lagrangian formulation is [4]

$$\dot{W} = \dot{W}_{\text{int}} - \dot{W}_{\text{ext}} = \int_\Omega \bar{W}d\Omega + \int_\Omega \tilde{W}d\Omega - W_{\text{ext}}, \tag{13}$$

3

where $\dot{W}_{int}$ and $\dot{W}_{ext}$ are the internal and external energies, respectively. Applying the Principle of Virtual Powers, there is a equilibrium state ϕ with kinematically admissible virtual velocities $\delta\mathbf{v}$, where

$$\delta\dot{W}(\phi, \delta\mathbf{v}) = \delta\dot{W}_{\text{int}} - \delta\dot{W}_{\text{ext}} = 0. \tag{14}$$

The internal power $\delta\dot{W}_{\text{int}}$ is

$$\delta\dot{W}_{\text{int}} = \int_{\Omega} \bar{\mathbf{S}} : \delta\dot{\mathbf{E}}d\Omega + \int_{\Omega} \tilde{\mathbf{S}} : \delta\dot{\mathbf{E}}d\Omega, \tag{15}$$

and $\delta\dot{W}_{\text{ext}}$ is the external power

$$\delta\dot{W}_{\text{ext}} = \int_{\Omega} \mathbf{f} \cdot \delta\mathbf{v}d\Omega + \int_{\Gamma} \mathbf{t} \cdot \delta\mathbf{v}d\Gamma, \tag{16}$$

where $\mathbf{f}$ and $\mathbf{t}$ are the body and surface forces, respectively. The weak form for the hydrostatic pressure is then defined

$$\int_{\Omega} (J-1)\delta q \, d\Omega = \frac{1}{K} \int_{\Omega} p\delta q \, d\Omega, \quad \forall \, \delta q \, \in \, L^2, \tag{17}$$

with L^2 being a Hilbert space with square integrable functions. Looking at Eq.17, one shall notice that as K approaches sufficiently high values, the condition $J \approx 1$ is enforced, reducing the volumetric deformation as much as possible. Thus, with the inclusion of this constraint completes the mixed formulation.

2.3   Linearization of the weak form

Taking the directional derivative of Eq.14 without considering a follower load, we have [4]

$$\mathcal{D}\delta W(\phi, \delta\mathbf{v})[\Delta\mathbf{u}] = \int_{\Omega} \left(\bar{\mathbf{S}} + \tilde{\mathbf{S}}\right) : \left[(\boldsymbol{\nabla}_0\Delta\mathbf{u})^T \boldsymbol{\nabla}_0\delta\mathbf{v}\right] d\Omega$$
$$+ \int_{\Omega} \frac{1}{2}\left[\mathbf{F}^T(\boldsymbol{\nabla}_0\delta\mathbf{v}) + \mathbf{F}(\boldsymbol{\nabla}_0\delta\mathbf{v})^T\right]^T : \left(\bar{\mathcal{C}} + \tilde{\mathcal{C}}\right) : \frac{1}{2}\left[\mathbf{F}^T(\boldsymbol{\nabla}_0\Delta\mathbf{u}) + \mathbf{F}(\boldsymbol{\nabla}_0\Delta\mathbf{u})^T\right] d\Omega. \tag{18}$$

Recalling the separation of $\tilde{\mathcal{C}}$ into $\tilde{\mathcal{C}}^{\mathbf{1}}$ and $\tilde{\mathcal{C}}^{\mathbf{2}}$ from Eq.12, the linearized functional can be rewritten as

$$\mathcal{D}\delta W(\phi, \delta\mathbf{v})[\Delta\mathbf{u}] = \int_{\Omega} \left(\bar{\mathbf{S}} + \tilde{\mathbf{S}}\right) : \left[(\boldsymbol{\nabla}_0\Delta\mathbf{u})^T \boldsymbol{\nabla}_0\delta\mathbf{v}\right] d\Omega$$
$$+ \int_{\Omega} \frac{1}{2}\left[\mathbf{F}^T(\boldsymbol{\nabla}_0\delta\mathbf{v}) + \mathbf{F}(\boldsymbol{\nabla}_0\delta\mathbf{v})^T\right]^T : \left(\bar{\mathcal{C}} + \tilde{\mathcal{C}}^{\mathbf{1}}\right) : \frac{1}{2}\left[\mathbf{F}^T(\boldsymbol{\nabla}_0\Delta\mathbf{u}) + \mathbf{F}(\boldsymbol{\nabla}_0\Delta\mathbf{u})^T\right] d\Omega$$
$$+ \int_{\Omega} \left[\frac{1}{2}\mathbf{F}^T(\boldsymbol{\nabla}_0\delta\mathbf{v}) + \mathbf{F}(\boldsymbol{\nabla}_0\delta\mathbf{v})^T\right] : J\mathbf{C}^{-1}\Delta p \, d\Omega. \tag{19}$$

The term Δp is a pressure increment

$$\Delta p = \frac{1}{2}KJ\mathbf{C}^{-1} : \left[\mathbf{F}^T(\boldsymbol{\nabla}_0\Delta\mathbf{u}) + \mathbf{F}(\boldsymbol{\nabla}_0\Delta\mathbf{u})^T\right], \tag{20}$$

resulting from the derivative $\frac{\partial p}{\partial\mathbf{E}}$ in $\tilde{\mathcal{C}}^{\mathbf{2}}$ (Eq.12).

4

2.4   Local Pressure Projection

The shape functions used to interpolate the kinematic variables and pressure are from a Lagrange nodal basis. There are known problems regarding the system conditioning when using high polynomial degrees and equally spaced nodes [17]. To avoid that, a more robust expansion can be obtained by calculating the polynomials at the Gauss-Lobatto-Legendre points.

The pressure projection procedure is performed at the element level, thus the variables are accompanied by a subscript ^{e}, denoting a local element. The projected terms are represented by the subscript *. Also, the shape functions used to interpolate the displacements are denoted by $\mathbf{N}$, with an associated interpolation order O_u. In the case of the hydrostatic pressure, we denote the shape functions as $\mathbf{Q}$ and the interpolation order as O_p.

Consider the approximation of $p^e(\mathbf{X})$ in a least squares sense using a linear combination of functions $\mathbf{Q} = \{Q_1(\mathbf{X}), Q_2(\mathbf{X}), ..., Q_n(\mathbf{X})\}$ in L^2. Hence, we should find $\mathbf{p}^e = [p_1^e, p_2^e, ..., p_n^e]$ that minimizes [4]

$$\phi(\mathbf{p}^e) = ||p^e - \mathbf{Q}\mathbf{p}^e||_{L_2(\Omega^e)}^2. \tag{21}$$

The term $p^e - \mathbf{Q}\mathbf{p}^e$ is a residual R

$$R = p^e - \mathbf{Q}\mathbf{p}^e. \tag{22}$$

The following projection problem is stated

$$\frac{\partial ||R||^2}{\partial \mathbf{p}^e} = \int_{\Omega^e} \frac{\partial R^2}{\partial \mathbf{p}^e} d\Omega^e = 0, \tag{23}$$

which yields the following linear system

$$\mathbf{M}^e \mathbf{p}^e = \mathbf{F}^e, \tag{24}$$

where $\mathbf{M}^e$ is a projection matrix and $\mathbf{F}^e$ is the right hand side vector containing the pressure

$$\mathbf{M}^e = \int_{\Omega^e} \mathbf{Q}^T \mathbf{Q} \, d\Omega^e, \tag{25}$$

$$\mathbf{F}^e = \int_{\Omega^e} \mathbf{Q}^T p^e \, d\Omega^e. \tag{26}$$

So, the projected hydrostatic pressure at the element level is

$$p^{e*} = \mathbf{Q}\mathbf{p}^e = \mathbf{Q}(\mathbf{M}^e)^{-1}\mathbf{F}^e. \tag{27}$$

For consistency, the same procedure is employed for the pressure increment Δp, leading to

$$\Delta p^{e*} = K\mathbf{Q}(\mathbf{M}^e)^{-1}(\mathbf{K}_p^e)^T \Delta \mathbf{u}^e, \tag{28}$$

and incorporating the mixed matrix $\mathbf{K}_p^e$

$$\mathbf{K}_p^e = \int_{\Omega^e} J\mathbf{Q}^T \mathbf{C}^{-1}\mathbf{B}_{\mathrm{NL}} \, d\Omega^e. \tag{29}$$

This matrix contains pressure and displacements shape functions, and is not necessarily a square matrix. The term $\mathbf{B}_{\mathrm{NL}}$ is the nonlinear Green deformation matrix

$$\mathbf{B}_{\mathrm{NL}} = \frac{1}{2}\left[\mathbf{F}^T(\boldsymbol{\nabla}_0 \Delta \mathbf{u}) + \mathbf{F}(\boldsymbol{\nabla}_0 \Delta \mathbf{u})^T\right]. \tag{30}$$

Algorithm 1 describes the pressure projection procedure performed at the integration points.

Algorithm 1 Pressure projection procedure.

1. Calculate the displacement based hydrostatic pressure $\tilde{p}^e$ (Eq.6) for all integration points;

2. Assemble the element projection matrix $\mathbf{M}^e$, using a pressure order O_p;

3. Assemble the right hand side vector $\mathbf{F}^e$, also with order O_p;

4. Solve the linear system (Eq.24) to find the pressure coefficients $\mathbf{p}^e$;

5. Compute the product $\mathbf{Q}\mathbf{p}^e$ to find the projected pressure p^{e*}.

2.5 Discretization of the equilibrium equations

The discretization of the equilibrium equation (Eq.13) leads to an element residual force $\mathbf{R}^e$ [3]

$$\mathbf{R}^e = \mathbf{f}^e_{\text{int}} - \mathbf{f}^e_{\text{ext}}. \tag{31}$$

where $\mathbf{f}^e_{int}$ and $\mathbf{f}^e_{ext}$ are the discretized internal and external forces at the element, respectively

$$\mathbf{f}^e_{\text{int}} = \int_{\Omega^e} \mathbf{B}^T_{\text{NL}} \left(\bar{\mathbf{S}}_v + \tilde{\mathbf{S}}_v \right) d\Omega^e, \tag{32}$$

$$\mathbf{f}^e_{\text{ext}} = \int_{\Omega^e} \mathbf{N}\mathbf{f} d\Omega^e + \int_{\Gamma^e} \mathbf{N}\mathbf{t} d\Gamma^e. \tag{33}$$

The discretization of the linearized equilibrium equation (Eq.19) yields the element tangent stiffness matrix [4]

$$\mathbf{K}^e_t = \bar{\mathbf{K}}^e + \tilde{\mathbf{K}}^e + \tilde{\mathbf{K}}^{e*}, \tag{34}$$

with

$$\bar{\mathbf{K}}^e = \int_{\Omega^e} \left(\mathbf{B}^T_\sigma \bar{\mathbf{T}}\mathbf{B}_\sigma + \mathbf{B}^T_{\text{NL}} \bar{\mathcal{D}}\mathbf{B}_{\text{NL}} \right) d\Omega^e, \tag{35}$$

$$\tilde{\mathbf{K}}^e = \int_{\Omega^e} \left(\mathbf{B}_\sigma^T \tilde{\mathbf{T}}\mathbf{B}_\sigma + \mathbf{B}_{\text{NL}}^T \tilde{\mathcal{D}}^1 \mathbf{B}_{\text{NL}} \right) d\Omega^e, \tag{36}$$

$$\tilde{\mathbf{K}}^{e*} = K \left(\mathbf{K}^e_p \right)^T \left(\mathbf{M}^e \right)^{-1} \left(\mathbf{K}^e_p \right). \tag{37}$$

The terms $\bar{\mathcal{D}}$ and $\tilde{\mathcal{D}}^1$ represent the matrix forms of $\bar{\mathcal{C}}$ and $\tilde{\mathcal{C}}^1$, respectively. $\mathbf{B}_\sigma$ is the initial stress matrix, which operates the geometric stiffness contribution. The matrices $\bar{\mathbf{T}}$ e $\tilde{\mathbf{T}}$ are composed by a Kronecker product between the stress and identity matrices

$$\bar{\mathbf{T}} = \bar{\mathbf{S}} \otimes \mathbf{I}, \tag{38}$$
$$\tilde{\mathbf{T}} = \tilde{\mathbf{S}} \otimes \mathbf{I}. \tag{39}$$

2.6 Global Newton-Raphson equation

After the definition of the element matrices, an assembly procedure is performed to obtain the global matrices. The global Newton-Raphson equation is given as [3]

$$\mathbf{K}^t_g \Delta\mathbf{u}_g = -\mathbf{R}_g, \tag{40}$$

where $\mathbf{K}_g^t$ and $\mathbf{R}_g$ are the global tangent stiffness matrix and the global residual force, respectively, and $\Delta \mathbf{u}_g$ is the global displacement increment.

The Newton-Raphson method is used to solve the incremental form of Eq.40 for the global displacements. According to [3], it is usually possible to obtain the solution by applying the external load directly. However, when treating large displacements, there may be some convergence issues. Thus, it is convenient to consider the application of external force increments

$$\mathbf{f}_{\text{ext}} = \sum_{i=1}^{l} \Delta \mathbf{f}_{\text{ext}}^i, \tag{41}$$

where $\Delta \mathbf{f}_{\text{ext}}$ is an external force increment, and l the total number of load increments.

The steps for solving the Newton-Raphson procedure are described by Algorithm 2.

Algorithm 2 Newton Raphson procedure

---

1. Given $\mathbf{u}$ for iteration k, compute the kinematic variables and perform the pressure projection described by Algorithm 1;

2. Update the stresses $\tilde{\mathbf{S}}$ and the volumetric part of the elasticity tensor $\tilde{\mathcal{C}}^1$ with the projected pressure $\mathbf{p}^{\mathbf{e}*}$;

3. Update the element stiffness matrices (Eqs.35, 36, 37), and the element internal force (Eq.32);

4. Assemble the global matrices and solve Eq.40 for $\Delta \mathbf{u}_g^k$, using a linear solver;

5. Update the displacements: $\mathbf{u}_g^{k+1} = \mathbf{u}_g^k + \Delta \mathbf{u}_g^k$;

6. Check the convergence criterion. If satisfied, go to the next load step. Or else, go to step 1.

---

3 DAMAGE MECHANICS

3.1 Damage variable and thermodynamic aspects

Consider a given material characterized by a deviatoric strain energy density $\bar{W}(\mathbf{E})$, subjected to a damaging deformation process. The starting point is the definition of the following damaged strain energy density [22, 14]

$$\bar{W}^D (\mathbf{E}, D) = (1 - D) \bar{W} (\mathbf{E}), \tag{42}$$

where $(1 - D)$ is the reduction factor introduced by [16] and D a scalar damage variable defined in

$$0 \leq D \leq 1. \tag{43}$$

When $D = 0$, the material is undamaged. The value $D = 1$ is an upper limit in which the material is completely damaged and failure occurs. The following observations must be made about this model:

1. The damage is isotropic and evolves coupled to the maximum attained strain;

2. The process is irreversible and independent of the loading nature. Hence, it is assumed that the effect of compressive and traction forces is the same to the damage evolution;

3. The material degradation occurs until a saturation of the damage parameter and can achieve a critical damage D_c.

3.2 Damage criterion and evolution

An equivalent strain related to the strain energy density is defined

$$\zeta_s = \sqrt{2\bar{W}\left(\mathbf{E}\left(t\right)\right)},\tag{44}$$

where $\mathbf{E}\left(t\right)$ is the Green-Lagrange strain tensor for the pseudo-time t of the deformation process. A maximum equivalent strain ζ_t^m until t is defined as

$$\zeta_t^m = \max_{t \in (-\infty, t]} \sqrt{2\bar{W}\left(\mathbf{E}\left(t\right)\right)}.\tag{45}$$

The damage criterion is analyzed using the following inequation

$$\psi\left(\mathbf{E}\left(t\right), \zeta_t^m\right) = \sqrt{2\bar{W}\left(\mathbf{E}\left(t\right)\right)} - \zeta_t^m \leq 0,\tag{46}$$

which defines a damage surface that grows isotropically with the deformation. If the above equation is satisfied, there is no need to update the damage variable. However, if $\psi > 0$, there is a damage evolution associated with the current deformation state, and the constitutive equations must be updated in a consistent manner.

The evolution of damage is described by a function $\bar{h}\left(\zeta\right) = -d\bar{g}\left(\zeta\right)/d\zeta$, with $\bar{g}\left(\zeta\right)$ being of an exponential form

$$\bar{g}\left(\zeta\right) = \beta + \left(1 - \beta\right)\frac{1 - e^{-\zeta/\alpha}}{\zeta/\alpha}.\tag{47}$$

The parameters $\beta \in [0, 1]$ and $\alpha \in [0, \infty)$ change according to the material. Fig.1 shows the form of the $\bar{g}$ function, by varying the parameters α and β. Fig.2 illustrates the derivative

$$\bar{g}'(\zeta) = (1 - \beta)\left[\frac{e^{-\zeta/\alpha}}{\zeta} - \frac{\alpha}{\zeta^2}\left(1 - e^{-\zeta/\alpha}\right)\right].\tag{48}$$

3.3 Constitutive relations

It is assumed that the evolution function $\bar{h}(\zeta_t)$ is independent of the damage variable, and the expression for the damaged stress $\mathbf{S}^D$ is written as [22]

$$\bar{\mathbf{S}}^D\left(t\right) = \bar{g}(\zeta_t^m)\frac{\partial \bar{W}(\mathbf{E})}{\partial \mathbf{E}}.\tag{49}$$

Recalling the stress reduction factor, the damage variable and the evolution function are related by

$$(1 - D) = \bar{g}(\zeta_t^m).\tag{50}$$

(a) Variation of α.　　　　　　　　(b) Variation of β.
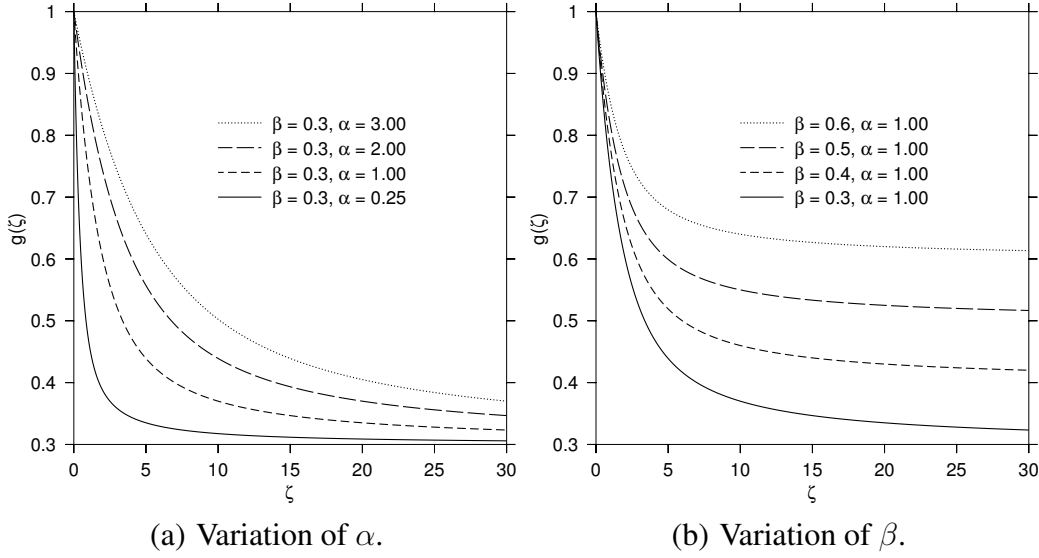
Figure 1: Function $\bar{g}$ in terms of the equivalent strain. Lower values for α characterize a faster decrease for the function, while keeping the asymptotic line. The parameter β defines the asymptotic value for the function, as seen on (b).

To find the complete constitutive relation, the following rate form is derived

$$\dot{\mathbf{S}}^D = \frac{\partial \bar{\mathbf{S}}^D}{\partial \mathbf{E}} : \dot{\mathbf{E}}. \tag{51}$$

Applying the chain rule, we have

$$\dot{\mathbf{S}}^D = \left(\bar{g}(\zeta_t^m) \frac{\partial^2 \bar{W}(\mathbf{E})}{\partial \mathbf{E}^2} + \frac{\partial \bar{g}(\zeta_t^m)}{\partial \zeta_t^m} \frac{\partial \zeta_t^m}{\partial \mathbf{E}} \otimes \frac{\partial \bar{W}(\mathbf{E})}{\partial \mathbf{E}} \right) : \dot{\mathbf{E}}, \tag{52}$$

so, the constitutive relation for the material with damage is obtained

$$\dot{\mathbf{S}}^D(t) = \begin{cases} \left[\bar{g}(\zeta_t^m) \bar{\boldsymbol{\mathcal{C}}} + \frac{\bar{g}'(\zeta_t^m)}{(\zeta_t^m)} \bar{\mathbf{S}} \otimes \bar{\mathbf{S}} \right] : \dot{\mathbf{E}}, & \text{if } \psi \geq 0 \\ \bar{g}(\zeta_t^m) \bar{\boldsymbol{\mathcal{C}}} : \dot{\mathbf{E}}, & \text{else.} \end{cases} \tag{53}$$

By looking at Eq.53, we shall notice the following: If there is no damage evolution, the reduction function $\bar{g}(\zeta_t^m)$ is applied to the deviatoric part of the constitutive tensor $\bar{\boldsymbol{\mathcal{C}}}$. Otherwise, an additional contribution of the derivative applied to the Kroenecker product of the stress tensor must be considered for consistency.

3.4 Damage algorithm

In order to update the constitutive equations used in the Newton-Raphson Method, a correct algorithmic procedure must be employed. The coupled equations are defined in a pseudo-time interval $[t_n, t_{n+1}]$, under the consideration of monotonic loading conditions.

- Deviatoric part of the right Cauchy-Green tensor:

$$\bar{\mathbf{C}}_{n+1} = \det F_{n+1}^{-2/3} \mathbf{C}_{n+1}. \tag{54}$$

9

(a) Variation of α.

(b) Variation of β.
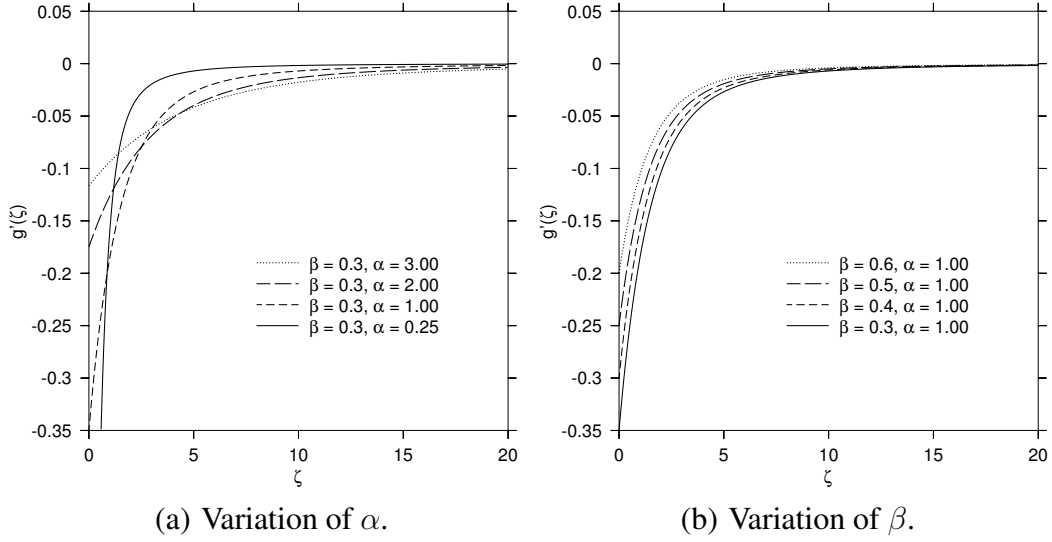
Figure 2: Derivative of the $\bar{g}$ function. For higher values of α the rate is smaller, and for lower values of α, the rate is higher.

- Invariants of $\bar{\mathbf{C}}_{n+1}$:

$$\bar{I}_{1,n+1} = J^{-2/3} I_{1,n+1}, \quad \bar{I}_{2,n+1} = J^{-4/3} I_{2,n+1}. \tag{55}$$

- Equivalent strain:

$$\zeta_{n+1} = \sqrt{2\bar{W}_{n+1}}. \tag{56}$$

- Damage surface:

$$\psi_{n+1} = \zeta_{n+1} - \zeta_n^m \le 0. \tag{57}$$

- Damage evolution law:

$$\bar{g}_{n+1}\left(\zeta_{n+1}\right) = \beta + (1 - \beta)\frac{1 - e^{-\zeta_{n+1}/\alpha}}{\zeta_{n+1}/\alpha}, \tag{58}$$

$$\bar{g}'_{n+1}(\zeta_{n+1}) = (1 - \beta)\left[\frac{e^{-\zeta_{n+1}/\alpha}}{\zeta_{n+1}} - \frac{\alpha}{\zeta_{n+1}^2}\left(1 - e^{-\zeta_{n+1}/\alpha}\right)\right]. \tag{59}$$

- Damage variable:

$$D_{n+1} = 1 - \bar{g}_{n+1}. \tag{60}$$

- Second Piola-Kirchhoff stress tensor:

$$\bar{\mathbf{S}}_{n+1}^D = \bar{g}_{n+1}\bar{\mathbf{S}}_{n+1} \tag{61}$$

- Tangent modulus without damage evolution:

$$\bar{\boldsymbol{\mathcal{D}}}_{n+1}^{ed} = \bar{g}_{n+1}\bar{\boldsymbol{\mathcal{D}}}_{n+1} \tag{62}$$

- Tangent modulus with damage evolution:

$$\bar{\boldsymbol{\mathcal{D}}}_{n+1}^{ed} = \bar{g}_{n+1}\bar{\boldsymbol{\mathcal{D}}}_{n+1} + \frac{\bar{g}'_{n+1}}{\left(\zeta_t^m\right)}\bar{\mathbf{S}}_{n+1} \otimes \bar{\mathbf{S}}_{n+1} \tag{63}$$

Algorithm 3 shows the steps for the stress and constitutive update procedure.

Algorithm 3 Update procedure for the damage formulation.

---

1. Given $\mathbf{F}_{n+1}$, ζ_t^m, $\bar{g}_n$ and D_n (Initial state or last converged iteration), calculate $\bar{\mathbf{C}}_{n+1}$ and the associated invariants.

2. Calculate the strain energy density $\bar{W}_{n+1}$;

3. Compute the equivalent strain ζ_{n+1} and damage surface ψ_{n+1}.

   If $\psi_{n+1} \leq 0$ Then

   No damage evolution:

   $\bar{g}_{n+1} = \bar{g}_n$

   $\bar{\boldsymbol{\mathcal{D}}}_{n+1}^{ed} = \bar{g}_{n+1}\bar{\boldsymbol{\mathcal{D}}}_{n+1}$

   Else

   Damage evolution:

   $\zeta_{n+1}^m = \zeta_{n+1}$

   Compute $\bar{g}_{n+1}$, $\bar{g}_{n+1}'$ e $\bar{\mathbf{S}}_{n+1}$, and $\bar{\boldsymbol{\mathcal{D}}}_{n+1}^{ed}$

4. Update the stresses $\bar{\mathbf{S}}_{n+1}^D$

---

4   Computational Tests

This section presents validation tests for a compressible Neo-Hookean material and a quasi-incompressible Mooney-Rivlin material, both coupled with damage. We used a nodal expansion basis with Lagrange polynomials calculated for Gauss-Legendre integration points and Gauss-Lobatto-Legendre collocation points.

The test geometry is a hexahedron shown by Fig.3, defined in $0 < X,\ Y,\ Z < 1\ m$. The face $X = 0$ is clamped. The domain was discretized using 1, 8, 27, 64 and 125 hexahedric finite elements.
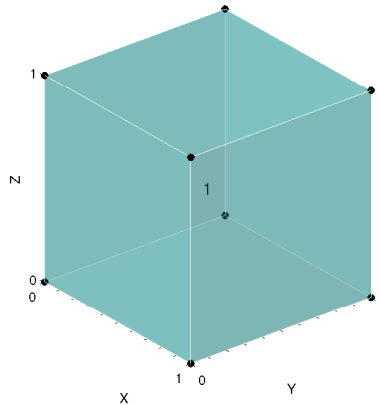
Figure 3: Hexahedric geometry.

(a) Second Piola-Kirchhoff stress.

(b) Cauchy stress.
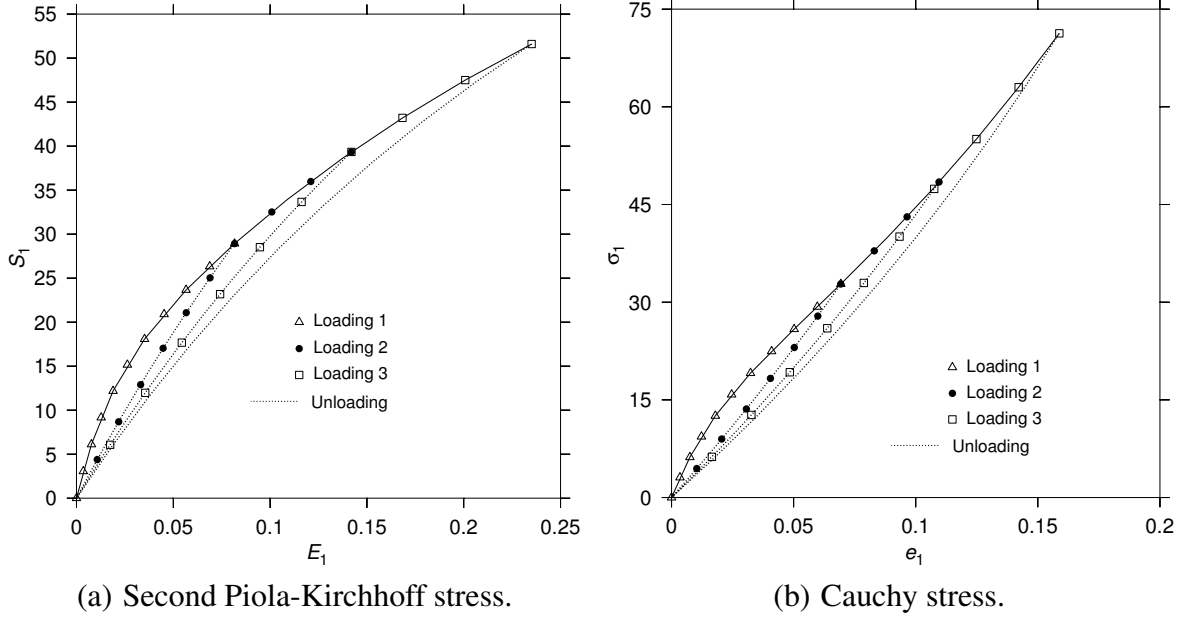
Figure 4: Mullins effect over the maximum principal stress. There is a progressive reduction of the stresses as the loading cycles are increased. At each reloading process, the stresses return to the main loading path, and the subsequent unloading depends on the new maximum achieved strain.

4.1 Test 1 - Damaged Neo-Hookean material

In order to analyze the Mullins effect, we performed a cyclic loading test using a Neo-Hookean material with damage. In this test, a pure displacement formulation is used, without the deviatoric/volumetric uncoupling, because the material is compressible and thus there is no locking tendency. The strain energy density form of the Neo-Hookean material is

$$W(\mathbf{C}) = \frac{\lambda}{2}(\ln J)^2 - \mu \ln J + \frac{1}{2}\mu(\mathrm{tr}\mathbf{C} - 3). \tag{64}$$

Three loading cycles are applied at face $X = 1$ with traction forces $t_1 = 35, \ 50, \ 75 \ N$. The following material properties are considered

$$E = 1000 \ Pa, \ \nu = 0.3, \ \alpha = 0.5, \ \beta = 0.3.$$

We used a single element mesh with interpolation order $O_u = 1$, and the maximum principal stress is analyzed for a given integration point. Fig.4(a) presents the maximum principal second Piola-Kirchhoff stress in terms of the maximum principal Green-Lagrange strain. Fig.4(b) shows the behavior of the maximum principal Cauchy stress in terms of the maximum principal Almansi strain.

The following step consists on a convergence test, using a smooth analytical solution and performing h and p refinements. In the case of the p type extension, we used a single element mesh, by varying the polynomial order from 1 to 9. In the case of a h type refinement, the interpolation is linear, using meshes of 1, 8, 27, 64 and 125 hexahedric elements. The analytic solution is

$$
\begin{aligned}
u_1 &= \sin(X), \\
u_2 &= 0, \\
u_3 &= 0,
\end{aligned}
\tag{65}
$$

which yields a displacement $u_1 \approx 0.84\ m$ in the face $X = 1\ m$. The body forces and traction fields are obtained from the continuity equation, and are not shown here because of the excessive size when considering the inclusion of damage. The damage parameters used are the following

$$\alpha = 1.0,\ \beta = 0.3.$$

Figs.5(a) and 5(b) show the L^2 error norm for the displacements, calculated for the entire domain, as

$$E_{L^2} = \sqrt{\int_\Omega \left(u_{analytic} - u_{approx}\right)^2\ d\Omega}. \tag{66}$$

A spectral convergence is achieved for the displacements in the p refinement, stagnating at 10^{-10} for $O_u \geq 8$. Figure 5(b) presents a comparison between both refinements, in terms of the total number of degrees of freedom.
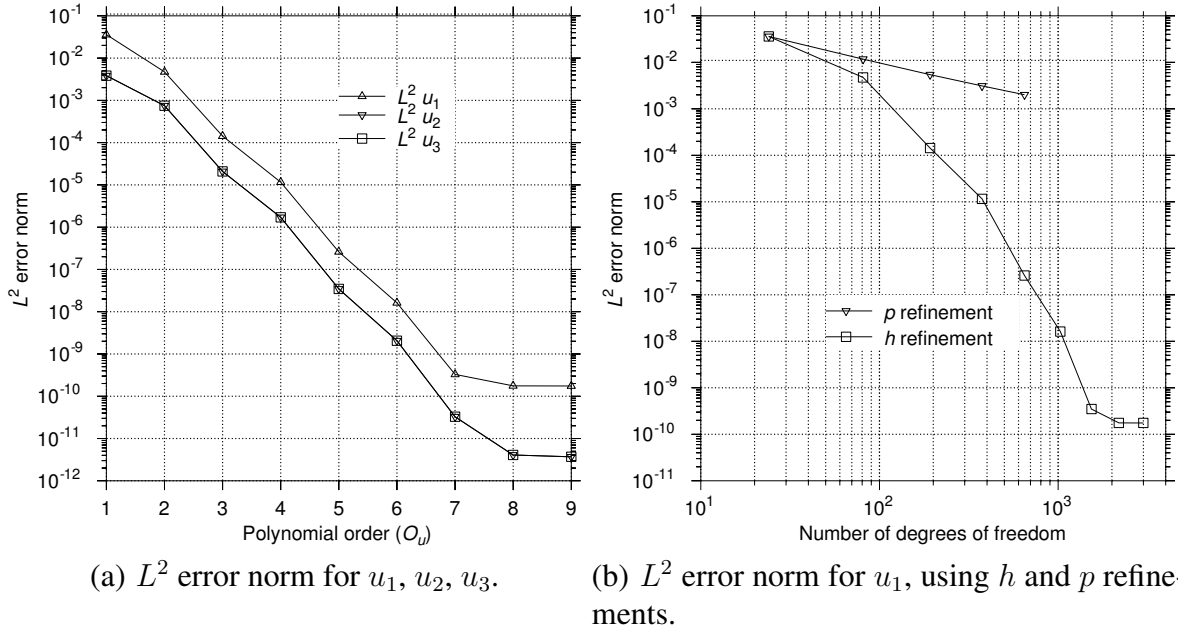
(a) L^2 error norm for u_1, u_2, u_3. (b) L^2 error norm for u_1, using h and p refinements.

Figure 5: L^2 error norm in terms of the interpolation order O_u (a), in terms of the total number of degrees of freedom (b). As expected for a smooth solution, the p refinement yields a spectral convergence, and the h refinement produces an algebraic convergence.

The displacement field u_1 and maximum principal stress σ_1 are shown by Fig.6. The nodal stress σ_1 and damage were also analyzed along the edge $Y = 0$, $Z = 0$, and are illustrated by Figs.7 and 8 with the analytic solution.

(a) u_1 displacement field.
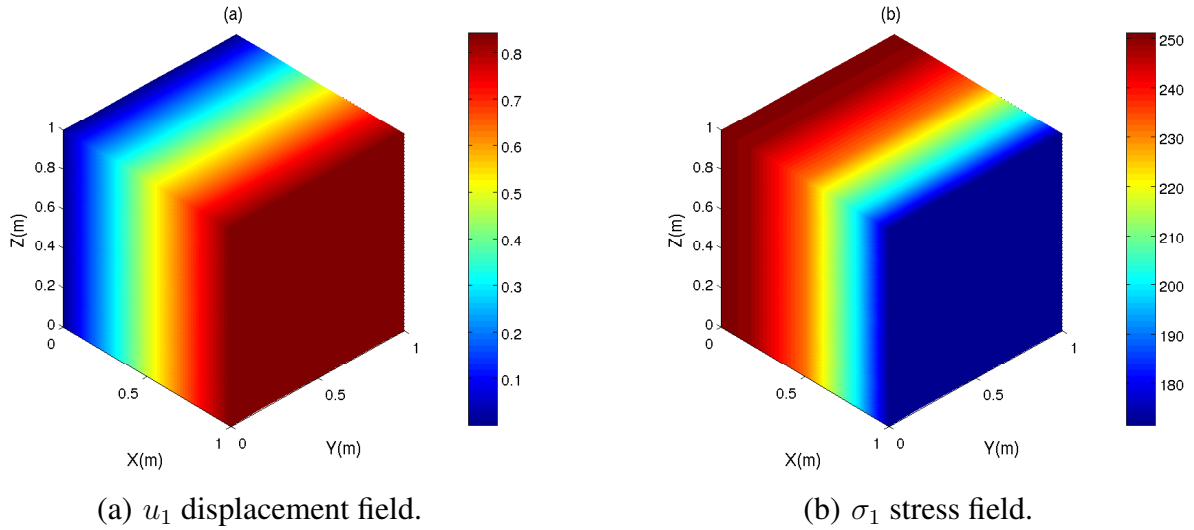
(b) σ_1 stress field.

Figure 6: Displacement field u_1 (a) and stress field σ_1 (b) using a single element mesh with $O_u = 3$.

Next, we calculated the absolute error for σ_1 and damage at the point $X, Y, Z = 0$, as

$$E_{abs,\sigma_1} = |\sigma_{1,analytic} - \sigma_{1,approx}|, \tag{67}$$

$$E_{abs,D} = |D_{analytic} - D_{approx}|. \tag{68}$$

Figure 9 illustrates the obtained results using a p refinement, by varying O_u from 1 to 8.
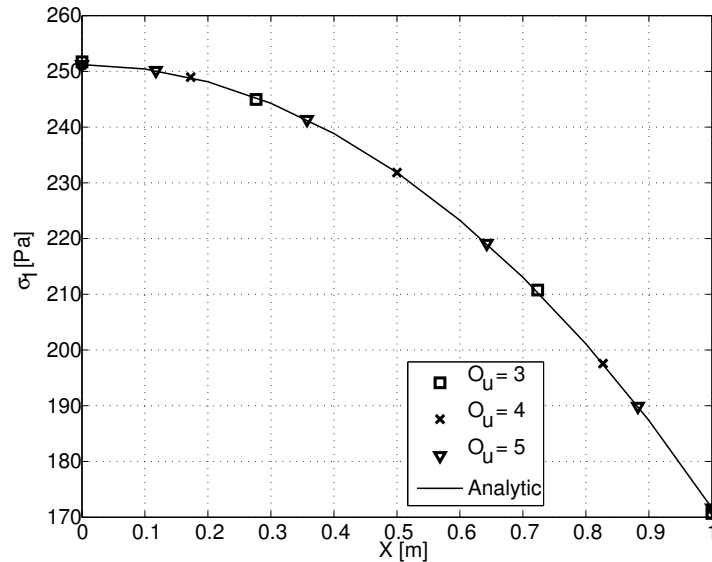
Figure 7: Approximated solution for σ_1 at the nodal points along the edge $Y = 0, Z = 0$.

14
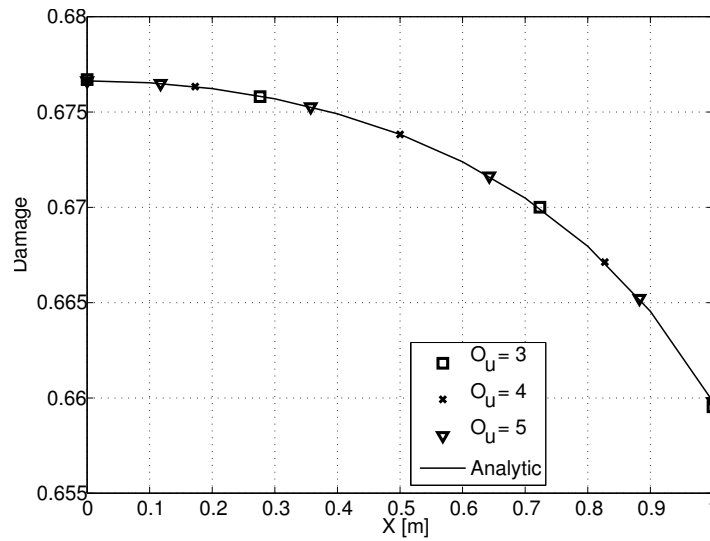
Figure 8: Approximated solution for damage at the nodal points along the edge $Y = 0$, $Z = 0$.
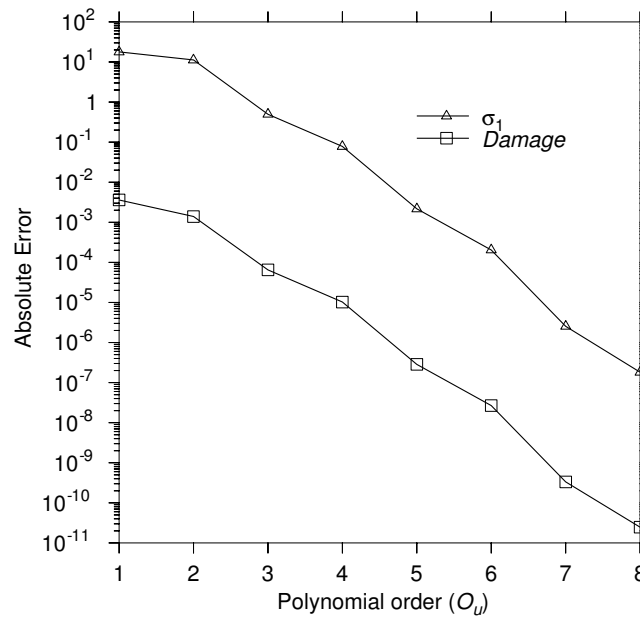
Figure 9: Absolute error for σ_1 and damage at the point $X, Y, Z = 0$. The convergence path is similar for both variables, but with a difference of about 4 orders of magnitude.

5 Test 2 - Damaged quasi-incompressible Mooney-Rivlin material

Our second test comprised the convergence behavior of a coupled damaged and quasi-incompressible Mooney-Rivlin material. The interpolation scheme used for the pressure was

$$O_p = O_u - 1. \tag{69}$$

The above relationship provides the best algorithmic stability, independently of the displacement order [24].

The following analytical solution was employed [24]

$$\begin{aligned} u_1 &= 0, \\ u_2 &= A\sin(BX), \\ u_3 &= 0, \end{aligned} \tag{70}$$

with

$$A = 0.25\ m,\ B = 1.0,$$

yielding a displacement $u_2 \approx 0.21$ in the face $X = 1$. Again, the applied loads are not presented due to the excessive size of the expressions with damage. The material properties are

$$A_{10} = A_{01} = 1.0\ Pa,\ K = 1.0 \times 10^3\ Pa,\ \alpha = 1.0,\ \beta = 0.3.$$

A h refinement was performed using 1, 8, 27, 64 and 125 hexahedric element meshes considering an interpolation order $O_u = 2$. Two types of p refinements were performed. The first one used a single element mesh, by varying the displacement order from 2 to 9 and consequently the pressure order from 1 to 8. The second used 8 elements, increasing the displacement order from 2 to 6 and the pressure order from 1 to 5. Fig.10 shows that in the case of quasi-incompressibility with damage, the convergence is harder than the compressible case. The L^2 norm for the displacements reduced exponentially until a stagnation starting at order $O_u = 5$ for the p refinement. The increase to 8 elements with the p refinement led to the same error magnitude, about 10^{-7}.
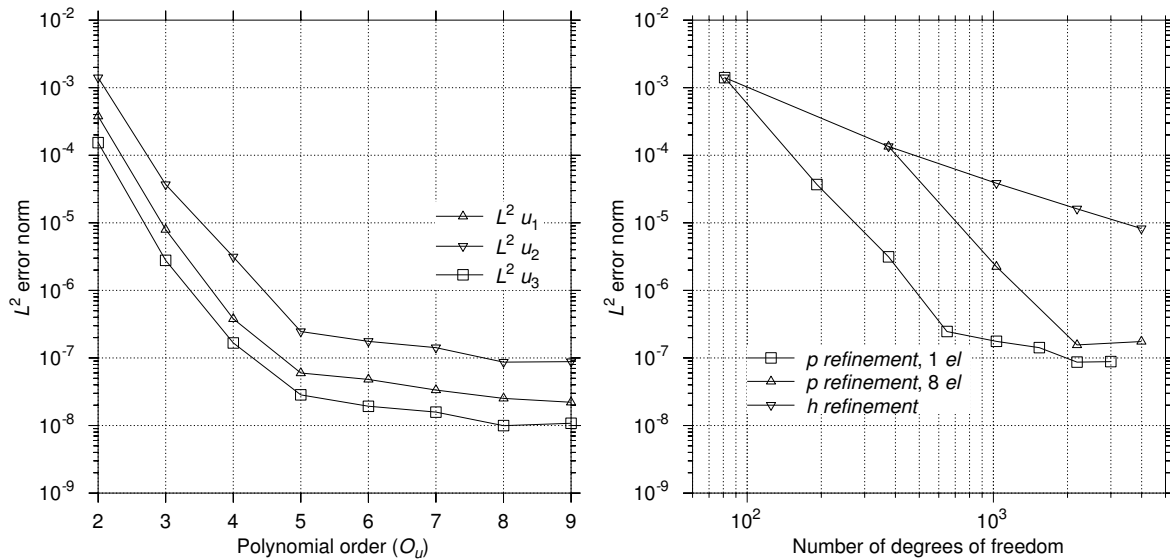
(a) L^2 error norm for u_1, u_2, u_3.   (b) L^2 error norm for u_2, h and p refinements.

Figure 10: L^2 error norm in terms of the displacement order (a), in terms of the total number of degrees of freedom (b).

Figs.11 and 12 present the maximum principal stresses and damage distributions along the edge $Y = 0$, $Z = 0$. The increase of the interpolation order and number of elements provided better results, but generally, the approximation is worse when compared to the compressible material.

16
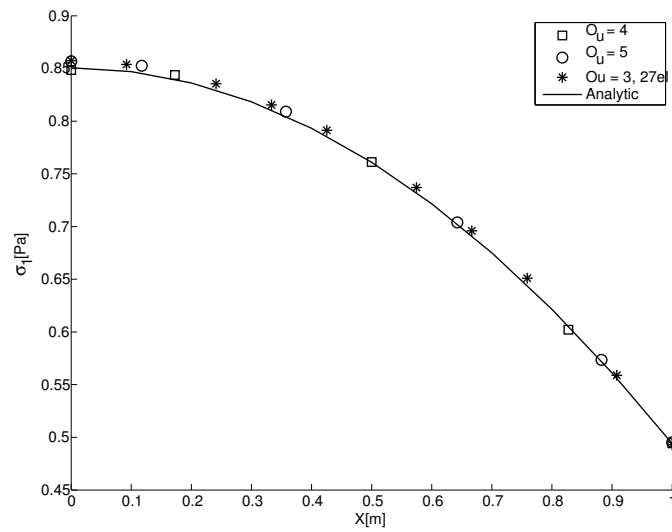
Figure 11: Approximated solution for the maximum principal stress σ_1 along the edge $Y = 0$, $Z = 0$.
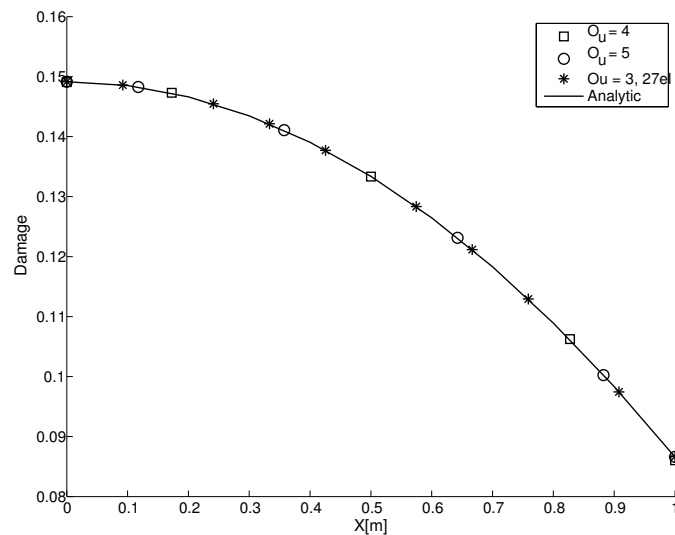
Figure 12: Approximated solution for damage along the edge $Y = 0$, $Z = 0$.

The absolute errors for σ_1 and damage at the point $X, Y, Z = 0$ were also computed for this test and are shown by Fig.13. There are no significant variations beyond the displacement order $O_u = 5$ for the stress, and at the same order the damage starts an oscillatory pattern. The maximum principal stress and damage fields are presented by Fig.14 for a 27 element mesh with $O_u = 3$.
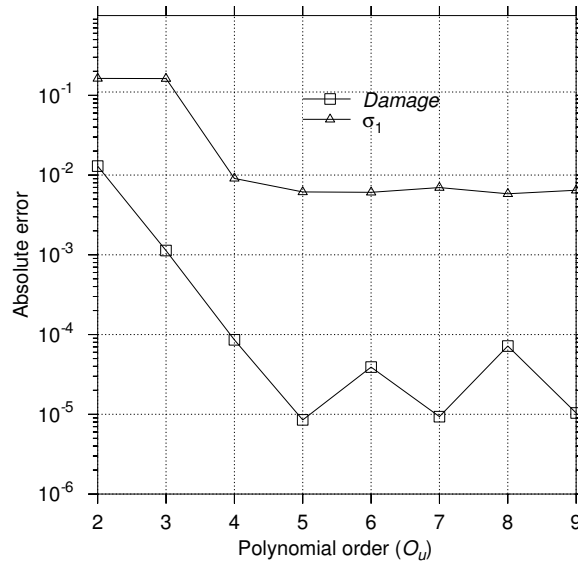
Figure 13: Absolute error for the principal stress σ_1 and damage at the point $X, Y, Z = 0$, using a p refinement.

(a) Principal stress σ_1.
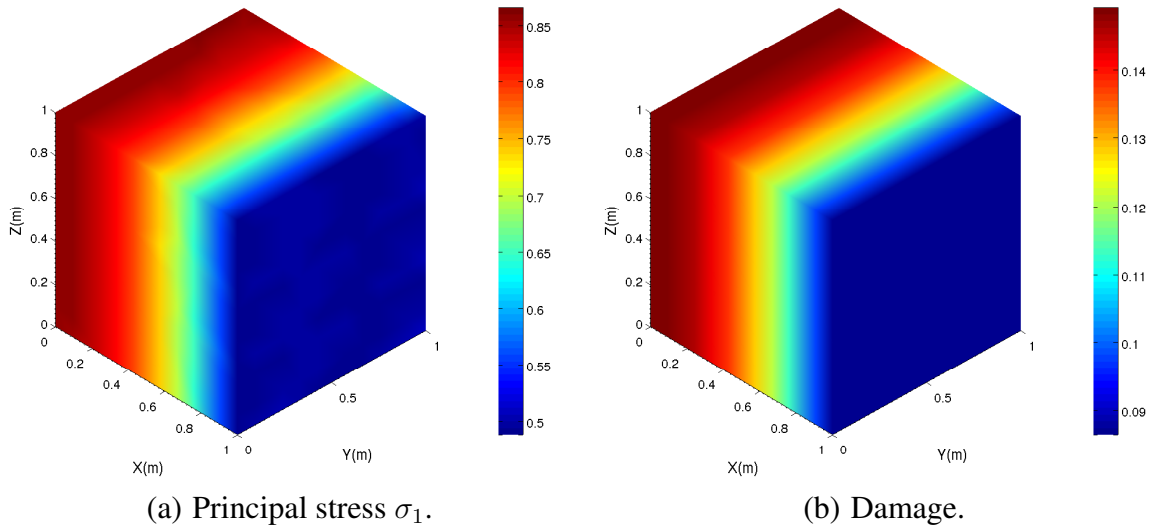
(b) Damage.

Figure 14: Maximum principal stress (a) and damage (b) distributions.

6   CONCLUSION

The coupling of a compressible hyperelastic material with damage led to a very good convergence for the p refinement, as expected since a smooth solution was considered. The errors for the stress are greater in magnitude compared to the damage. The Mullins effect could be reproduced with the application of a cyclic loading test, and showed a reduction of the material stiffness, depending on the maximum attained equivalent strain.

In the case of quasi-incompressibility with damage, we could overcome the locking behavior with the present formulation, combined with the increase of the polynomial order. However, the

convergence is more difficult, and no advantage could be noticed for the approximated solution with an interpolation order higher than $O_u = 5$.

The convergence difficulties related to large displacements can be avoided by partitioning the external load in incremental smaller values. It should be observed that this partitioning must consider sufficiently small values to avoid oscillations of the approximated solution.

References

[1] K.J. Bathe. *Finite element procedures*. Prentice Hall, 1996.

[2] A.A. Bendre. *Finite element analysis and preliminary experiments to study the effects of high myopia in macular degeneration*. Northeastern University, 2009.

[3] J. Bonet and R.D. Wood. *Nonlinear Continuum Mechanics for Finite Element Analysis*. Cambridge University Press, 1997.

[4] Jiun-Shyan Chen and Chunhui Pan. A pressure projection method for nearly incompressible rubber hyperelasticity, part i: Theory. *Journal of Applied Mechanics*, 63(4):862–868, 1996.

[5] E.A. de Souza Neto, D. Perić, M. Dutko, and D.R.J. Owen. Design of simple low order finite elements for large strain analysis of nearly incompressible solids. *International Journal of Solids and Structures*, 33(20-22):3277 – 3296, 1994.

[6] E.A. de Souza Neto, D. Perić, M. Dutko, and D.R.J. Owen. A phenomenological three-dimensional rate-independent continuum damage model for highly filled polymers: formulation and computational aspects. *J. Mech. Phys. Solids*, 42(10):1533 – 1550, 1994.

[7] E.A. de Souza Neto, D. Peric, and D.R.J. Owen. *Computational Methods for Plasticity: Theory and Applications*. John Wiley & Sons, 2011.

[8] S. Dong and Z. Yosibashi. A parallel spectral element method for dynamic three-dimensional nonlinear elasticity problems. *Computers and Structures*, 87:59–72, 2009.

[9] I. Fried. Finite element analysis of incompressible material by residual energy balance. *International Journal of Solids and Structures*, 10:993 – 1002, 1974.

[10] Y.-C. Fung. *Biomechanics: Mechanical Properties of Living Tissues*. Springer-Verlag, New York, 1993.

[11] M. E Gurtin and E. C Francis. Simple rate-independent model for damage. *J. Spacecraft*, (18):285–286, 1981.

[12] U. Heisserer, S. Hartmann, and D˙ On volumetric locking-free behaviour of p-version finite elements under finite deformations. *Communications in numerical methods in engineering*, 2007.

[13] U. Heisserer, S. Hartmann, A. Düster, Z. Yosibash, W. Bier, and E. Rank. p-fem for finite deformation powder compaction. *Comput. Methods Appl. Mech. Engrg*, 197:727–740, 2008.

[14] G.A. Holzapfel. *Nonlinear solid mechanics: a continuum approach for engineering*. Wiley, 2000.

[15] T.J.R. Hughes. *The finite element method: linear static and dynamic finite element analysis*. Dover Civil and Mechanical Engineering Series. Dover Publications, 2000.

[16] L.M. Kachanov. *Time rupture process under creep conditions*. Izv Akad Nauk SSR, 1958.

[17] G.E. Karniadakis and S.J. Sherwin. *Spectral/hp Element Methods for Computational Fluid Dynamics*. Numerical Mathematics and Scientific Computation. Oxford University Press, USA, 2005.

[18] A. Konyukhova and K. Schweizerhof. Incorporation of contact for high-order finite elements in covariant form. *Computer Methods in Applied Mechanics and Engineering*, 198:1213–1223, 2009.

[19] L Mullins. Softening of rubber by deformation. *Rubb. Chem. Technol*, (42):339 – 351, 1969.

[20] R.W. Ogden. *Non-Linear Elastic Deformations*. Dover Civil and Mechanical Engineering Series. Dover Publications, 1997.

[21] E.D. Power. *A nonlinear finite element model of the human eye to investigate ocular injuries from night vision goggles*. Virginia tech, 2001.

[22] J.C. Simo. On a fully 3-dimensional finite strain viscoelastic damage model - formulation and computational aspects. *Computer methods in applied mechanics and engineering*, 60(2):153 – 173, 1987.

[23] Z. Yosibash, S. Hartmann, U. Heisser, A. Dster, E. Rank, and M. Szanto. Axisymmetric preassure boundary loading for finite deformation analysis using p-fem. *Comput. Methods Appl. Mech. Engng*, 196:1261–1277, 2007.

[24] Yue Yu, Hyoungsu Baek, Marco L. Bittencourt, and George Em Karniadakis. Mixed spectral/hp element formulation for nonlinear elasticity. *Computer Methods in Applied Mechanics and Engineering*, 213-216(0):42 – 57, 2012.